CONF-950793--37

UCRL-JC-121200
PREPRINT

X-ray Laser Interferometry for Probing High-density Plasmas

A. S. Wan, L. B. Da Silva, T. W. Barbee, Jr., R. Cauble, P. Celliers,
S. B. Libby, R. A. London, J. C. Moreno, J. E. Trebes, F. Weber
Lawrence Livermore National Laboratory
Livermore, CA 94550, USA

This paper was prepared for submittal to the
SPIE, The International Society for Optical Engineering
40th Annual Meeting, San Diego, CA,
July 9-14, 1995

June 1995

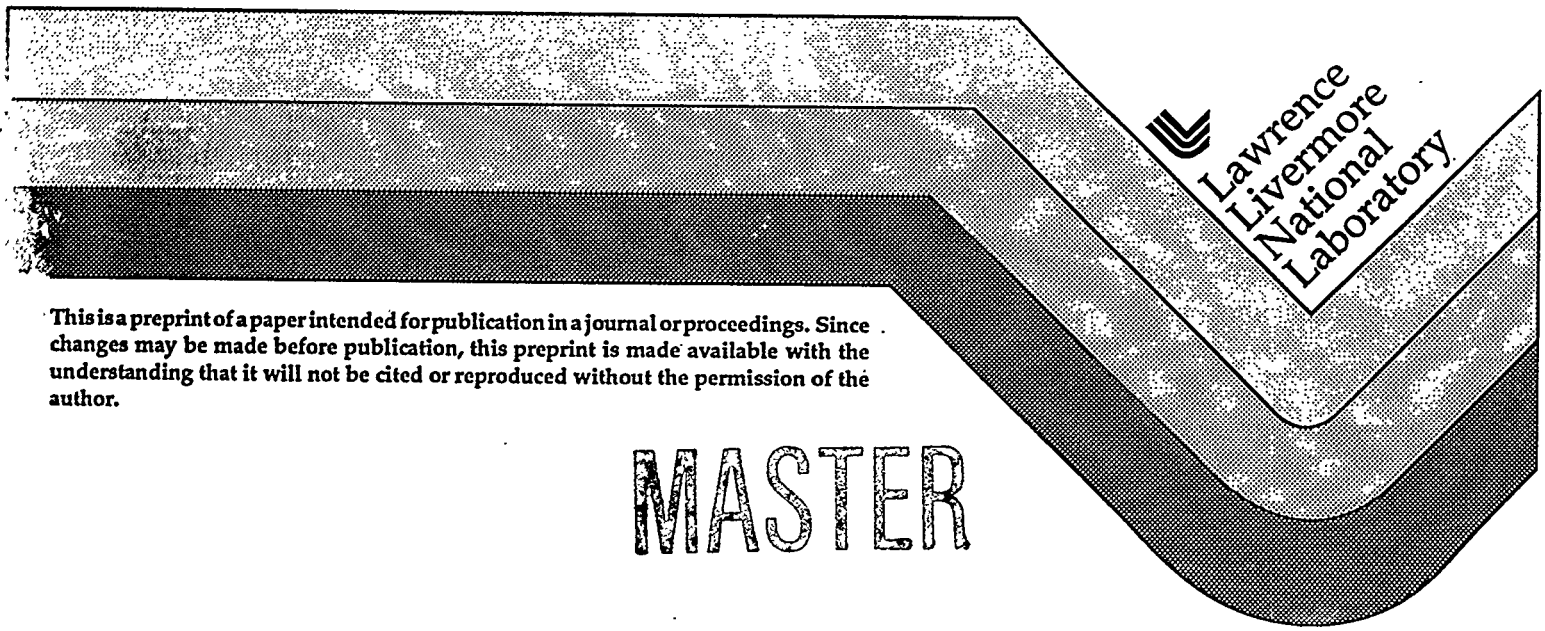

DISCLAIMER

DISCLAIMER

Portions of this document may be illegible in electronic image products. Images are produced from the best available original document.

X-ray Laser Interferometry for Probing High-density Plasmas

A. S. Wan, L. B. Da Silva, T. W. Barbee, Jr., R. Cauble, P. Celliers,
S. B. Libby, R. A. London, J. C. Moreno, J. E. Trebes, F. Weber

Lawrence Livermore National Laboratory, Livermore, CA 94550, U.S.A.

ABSTRACT

Collisionally pumped soft x-ray lasers now operate over a wavelength range extending from 4 - 40 nm. With the recent advances in the development of multilayer mirrors and beamsplitters in the soft x-ray regime, we can utilize the unique properties of x-ray lasers to study large, rapidly evolving laser-driven plasmas with high electron densities. Using a neon-like yttrium x-ray laser which operates at a wavelength of 15.5 nm, we have performed a series of x-ray laser interferometry experiments to characterize plasmas relevant to inertial confinement fusion. In this paper we describe experiments using a soft x-ray laser interferometer, operated in the Mach-Zehnder configuration, to study CH plasmas and exploding foil targets commonly used for x-ray laser targets. The two-dimensional density profiles obtained from the interferograms allow us to validate and benchmark our numerical models used to study the physics of laser-plasma interactions.

Keywords: x-ray laser, interferometry, applications, laser-plasma interactions

1. INTRODUCTION

Since the first demonstration of a soft x-ray laser,[1,2] x-ray lasers have been considered for applications in the fields of microscopy, holography, material science, and plasma physics.[3] With its short wavelength (4–40 nm), short controllable pulse duration, high peak brightness, and sufficient spatial and temporal coherence, the x-ray laser is ideally suited as a plasma diagnostic to image rapidly evolving (< 1 ns) laser-driven plasmas with high electron densities (10^{21} cm^{-3} < n_e < 10^{24} cm^{-3})

With recent advances in the development of short wavelength multilayer mirrors and beamsplitters in the soft x-ray regime,[4] we are pioneering the development and applications of x-ray lasers as imaging diagnostics for laser plasmas. Using x-ray lasers as high fluency monochromatic radiographic sources, radiographic images of smooth-laser accelerated foils have shown small-scale (~10 μm) filamentation which may reveal limitations to direct-drive inertial confinement fusion (ICF) capsules due to unexpectedly intense hydrodynamic instabilities.[5] We have also used x-ray lasers to measure 1-D density gradients of laser plasmas using the Moiré deflectometry technique.[6]

This paper is focused on the application of x-ray lasers to obtain absolute measurements of electron density using a soft x-ray laser interferometer. The size and density regime of the laser plasma accessible to an interferometer are limited by inverse bremsstrahlung absorption and refractive propagation of probe beams facing large density gradients. By employing a shorter wavelength x-ray laser, as compared to using conventional optical lasers as the probe source, we can access a much higher density regime while reducing refractive effects which limit the spatial resolution and data interpretation.

Extending conventional interferometric techniques into the soft x-ray range has been difficult because of the problems with designing optical systems which operate in the range

4-40 nm. Fortunately, multilayer mirror technology has now evolved to the point where artificial structures can be routinely fabricated with reflectivities as high as 65% at 13 nm,[7,8] and with the overall uniformities required by more conventional interferometers. We have also successfully fabricated high quality, large active area (1.2 cm x 1.2 cm) beamsplitters with excellent reflectivity and transmission at short wavelengths. Utilizing these multilayer optical components and a collisionally pumped neon-like yttrium x-ray laser operating at 15.5 nm as the probe source, we have successfully demonstrated a soft x-ray laser interferometer in a skewed Mach-Zehnder configuration.

The applicability of the soft x-ray laser interferometry technique to study the physics of laser-produced plasmas is the primary focus of this paper. In section 2 we briefly describe the setup of the soft x-ray laser interferometer at 15.5 nm using a yttrium x-ray laser. In section 3 we describe the numerical methodology for simulating the laser-produced plasmas and discuss issues that are relevant to data analysis. We have measured electron densities exceeding 2 x 10^{21} cm^{-3} in a CH plasma which is millimeters in extent and we will present that result in section 4. In section 5 we will describe our measurement of the density profile of a Se exploding foil commonly used for x-ray laser targets. We summarize and outline our future research direction in section 6.

2. EXPERIMENTAL SETUP

The experimental setup used to probe plasmas is shown schematically in Figure 1. The system consists of a collimated x-ray laser source, an imaging mirror and a skewed Mach-Zehnder interferometer. In order to reduce background self-emission, a series of three multilayer mirrors were used prior to the CCD detector, reducing the bandpass of the system. The effective bandpass of this system was 0.4 nm, which is significantly broader than the 0.001 nm spectral width of the x-ray laser source. The image magnification was 19 giving a pixel limited resolution of ~1.3 μm. Reference 9 gives a detailed description of the instrumentation.

The transmissive and reflective properties of the multilayer components, at the appropriate wavelength and operating angles, were characterized prior to the experiment.

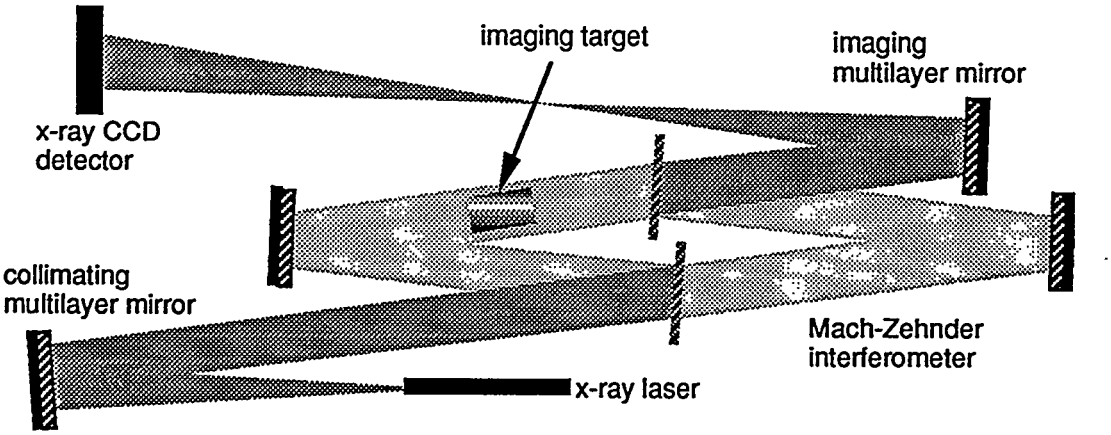

Figure 1. Experimental setup of the soft x-ray laser interferometer system which consists of a collimated x-ray laser source, an imaging mirror and an interferometer in a skewed Mach-Zehnder configuration.

The multilayer mirrors have a peak reflectivity of 60±5% at 15.5 nm. The beamsplitters used in the interferometer are the most critical element of the system. The measured reflectivity and transmission for these beamsplitters at 15.5 nm were 20% and 15% respectively. The overall throughput of each arm, accounting for the mirror and beamsplitter (one transmission & one reflection), was ~ 0.6 x 0.20 x 0.15 = 18%.

A collisionally pumped neon-like yttrium x-ray laser operating at 15.5 nm was used as the probe source. The x-ray laser was produced by irradiating a solid 3-cm-long yttrium target with one beam from Nova (0.53 μm, 600-ps-long square pulse) at an intensity of 1.5×10^{14} W/cm^2. The x-ray laser has an output energy of 3±2 mJ, a FWHM divergence of ~10-15 mrad and an output pulse width of 350 ps. The short pulse and high brightness of the x-ray laser allowed us to obtain an interferogram in a single 350 ps exposure thereby reducing the effects of vibrations and motion blurring. The timing between the two Nova lasers, one to generate the x-ray laser and one to produce the target plasma, was defined by the time-of-flight path of our interferometer setup and the desired probe time. Reference 10 describes the measurement of the transverse and temporal coherence properties of the x-ray laser which are important in the design of our interferometer.

3. NUMERICAL SIMULATIONS & DATA ANALYSIS

3.1 Data Analysis

The index of refraction of a plasma, n_{ref}, is related to the critical electron density, $n_{cr} = 1.1 \times 10^{21} \lambda^{-2}$ [cm^{-3}] by $n_{ref} = \sqrt{1 - n_e/n_{cr}}$, where λ is the probe laser wavelength in μm. In an interferometer the number of fringe shifts, N_{Fringe}, is then given by

$$N_{Fringe} = \frac{\delta\phi}{2\pi} = \frac{1}{\lambda}\int_0^L (1 - n_{ref})\, dl \approx \frac{n_e}{2n_{cr}}\frac{L}{\lambda}, \qquad (1)$$

where L [μm] is the path length across the target plasma and we assume refraction effects are negligible. Experimentally we measured N_{Fringe}, or in effect we measured the $(n_e L)$ product. To deduce n_e, we need to know L, which is sensitively dependent on the hydrodynamic expansion of the laser plasma. We will further discuss the our data analysis for deducing n_e for the experimental configurations described in Sec. 4 and 5.

3.2 Methodology for Numerical Modeling

Since the laser-produced plasma expands in three dimensions, we do not have a well-defined path length to use for data analysis and must rely on further numerical simulation to analyze the measured interferogram. We use LASNEX[11] in an axisymmetric two-dimensional (2-D) configuration for our data analysis.

LASNEX includes many physics models necessary to simulate a multi-dimensional radiative hydrodynamics problem, including laser-matter interaction, radiation transfer, electron thermal diffusion by conduction, and simple description of non-local thermodynamic equilibrium atomic kinetics. Reference 11 includes a description of the physics models used in LASNEX. The LASNEX parameters used are based on simulations that yielded the best agreements between simulations and past experiments. These parameters may vary depending on the physical regime of the problem. For example, in LASNEX, we employ a flux-limited thermal diffusion model for the electron energy transport. The value of the flux limiter determines the degree of the artificial reduction of the thermal flux. Past studies[12,13,14,15,16] have found that by varying the flux

limiter, which can range from strongly flux-limited diffusion to no reduction, better agreements between simulated and measured profiles of temperatures, densities, and x-ray conversion can be achieved. It is the validity and benchmarking of these numerical models, with the absolute n_e measurements at high densities, that are the primary reasons for performing experiments using x-ray laser interferometry.

4. TRIANGULAR CH TARGET

The setup of our first proof-of-principle experiment is shown in Figure 2. The target was a silicon wafer overcoated with 10 μm of CH and was in the shape of an isosceles triangle to allow a range of plasma path lengths to be probed simultaneously. The silicon substrate was polished to ~0.7 nm rms roughness to produce a clean flat surface. The optical laser incident the CH target from the +y direction, with $x = 0$ defined as the tip of the triangle.

The CH side was irradiated with a beam smoothed with random phase plates and segmented with wedges to produce a flat-top intensity distribution over a 0.7 mm diameter spot.[17] The drive pulse has a 1-ns-long, temporally square pulse profile with a wavelength of 0.53 μm. Thirty percent of the beam energy was concentrated within the 0.7 mm diameter spot producing an intensity on target of 2.7×10^{13} W/cm^2. The rest of the beam energy was spread over a larger area as shown in Fig. 2. Therefore, beyond $x =$ 0.35 mm we longer have a clean illumination geometry. Figure 2 also shows the alignment of the 0.7 mm spot with respect to the triangular target. However, there is some degree of uncertainty in this spatial alignment. In such a three-dimensional (3-D) configuration, the relative geometry of the laser focus and the target is an important consideration for data analysis and contributes to the uncertainty of the measured density profiles.

The target was backlit edge-on by the x-ray laser beam 1.1 ns after the start of the laser pulse that generated the CH plasma. The collimated x-ray laser beam was several millimeters in extend and was directed parallel to the z-axis. The side view of Fig. 2 shows the view along the z-axis, in the direction of the x-ray laser probe beam.

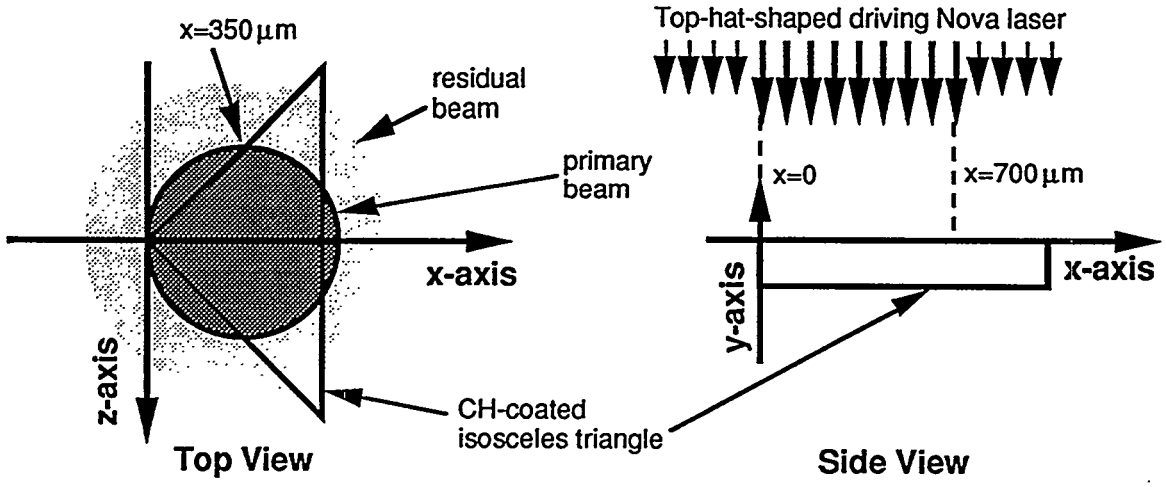

Figure 2. Geometry and definition of coordinate system of the triangular-shaped CH target which allows simultaneous probing of a range of plasma path lengths. The top view shows the spot of the driving laser, incident parallel to the y-axis with $x = 0$ defined as the tip of the triangle. The target was backlit edge-on by the x-ray laser beam 1.1 ns after the start of the laser pulse that generated the CH plasma. The collimated x-ray laser beam was several millimeters in extent and was directed parallel to the z-axis.

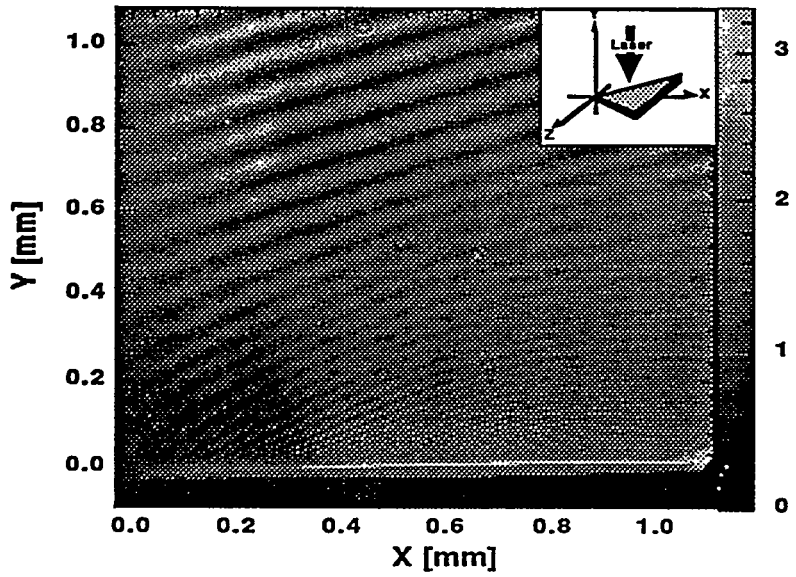

Figure 3. Interferogram of the CH plasma. Fringes are resolved as close as 0.025 mm from the initial target surface. Null fringes are visible in the perimeter. The scale at the right edge of the image indicates the relative intensities.

In Fig. 3 we show the interferogram of the CH plasma, in the x-y geometry defined by the side view of Fig. 2. The image shows excellent fringe visibility and very little self emission from the plasma. Fringes are resolved as close as 0.025 mm from the initial target surface. Close to the critical surface ($n_{cr} \sim 4 \times 10^{21}$ cm^{-3} for 0.53 μm driving laser wavelength), the fast evolution of the density profile and large density gradient cause motion blurring of the fringes within the 350 ps x-ray laser frame time. At the perimeter of the interferogram we can still see the unperturbed fringe pattern where there is no plasma. We can use these unperturbed fringes to reconstruct a unperturbed fringe mapping for the entire coverage. We can then use that reconstructed mapping as a reference to measure the amount of fringe shift due to the presence of the CH plasma. The beamsplitters were not perfectly flat, creating some minor variations in the unperturbed fringe pattern and that is one of our dominant experimental uncertainties. Based on previous null shots with similar quality beamsplitters, we estimate the uncertainty to be of order 0.1 fringe.

Once we measure the fringe shifts, we can then use Eqn. 1 to reconstruct a 2-D n_e profile. The lone remaining unknown is the plasma path length. If we assume that the plasma is confined to a one-dimensional (1-D) expansion in the y-direction, then the path length of a 1-D expanded isosceles triangular target can be simply defined as the width of the isosceles triangle, or L_{slab}, and the fringe shift should vary linearly with the distance away from the tip of the triangle. Using this simplified assumption we plot in Fig. 4 the measured n_e profiles, or n_e^{meas}, as a function of the blowoff direction y, at $x = 0.05$, 0.1, 0.2, and 0.35 mm.

Using 1-D geometries to simulate this experiment results in significant discrepancy due to the unconfined 3-D expansion of the CH plasma. This 3-D effect should be more pronounced near the triangle tip, and significant lateral expansion leads to lower electron densities as observed in Fig. 4. Reference 18 describes in detail comparisons of the calculated density profiles between 1-D and 2-D simulations for such laser-produced plasmas. In a 1-D wedge geometry, we allow the boundary of the laser plasma to expand in the transverse direction at a defined angle in order to approximate the effect of 2-D hydrodynamic expansion. The 1-D simulation results, using different wedge

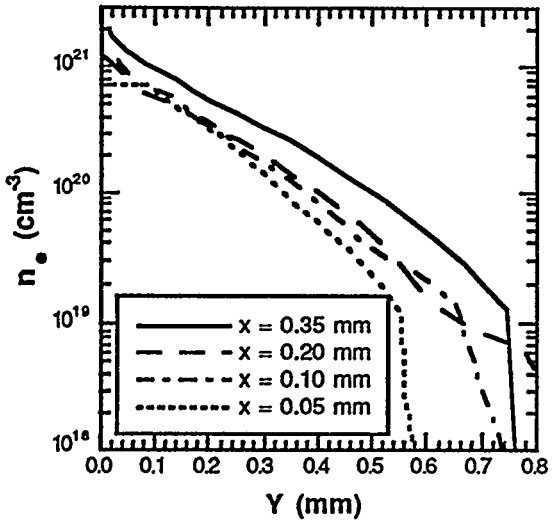

Figure 5. The measured n_e profiles as a function of the blowoff direction y, at x = 0.05, 0.1, 0.2, and 0.35 mm.

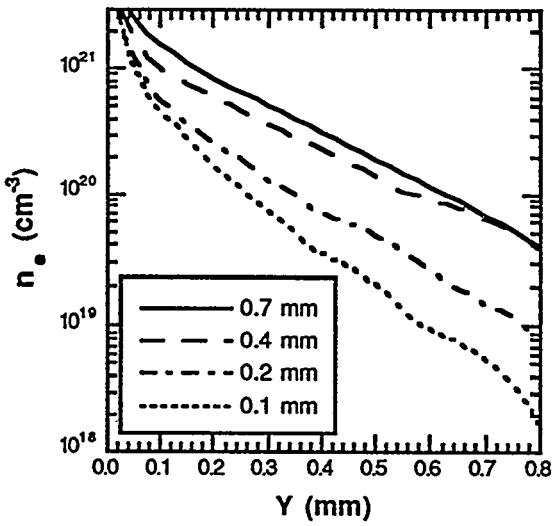

Figure 6. $[n_e]^{cal}$ profiles using finite slab widths of 0.1, 0.2, 0.4, and 0.7 mm. These $[n_e]^{cal}$ profiles correspond to the experimental positions of x = 0.05, 0.1, 0.2, and 0.35 mm (Fig. 5), with x = 0 defined as the tip of the isosceles triangle.

approximations, bracket the measured n_e profiles, but we cannot obtain satisfactory agreement between the data and the 1-D simulation results.

To account for the 2-D effect, we can then average the n_e along the z-direction, in the direction of the x-ray laser probe across a finite dimension slab. Since the total (n_e L) product should be conserved, we can derive an "averaged" calculated n_e profile, or $[n_e]^{cal}$, using the following formula:

$$[n_e(y)]^{cal} \equiv (L_{slab}(y))^{-1} \int_0^{L_p} n_e^{cal}(y,z)\, dz\,, \qquad (2)$$

where n_e^{cal} is our calculated 2-D n_e profile in the y- and z-directions, and L_p is the extent of the plasma expansion in the z-direction. Now $[n_e]^{cal}$ is a calculated n_e profile, in the direction of plasma blowoff (y-direction in our geometry), which is a better representation of the 2-D expansion effect than using simple 1-D wedge geometries. We can now use $[n_e]^{cal}$ to compare with an experimentally measured n_e profile, or n_e^{meas}, which is derived using the same $L_{slab}(y)$ quantity as the path length. This method represent our best estimate of the effect of multi-dimensional hydrodynamic expansion for most of the plasma region. The uncertainty is much larger near the critical surface where the density gradient is large and the profile changes rapidly.

Figure 6 is a plot of $[n_e]^{cal}$ profiles using finite slab widths of 0.1, 0.2, 0.4, and 0.7 mm. These $[n_e]^{cal}$ profiles correspond to the experimental positions of x = 0.05, 0.1, 0.2, and 0.35 mm, which are plotted in Fig. 5. Despite our attempt at accounting for the effect of multi-dimensional hydrodynamic expansion, we still observe disagreements between the n_e^{meas} profiles and the corresponding $[n_e]^{cal}$ profiles. At x = 0.35 and 0.2 mm, where our 1-D and 2-D comparisons suggest that the hydrodynamic effect should be negligible, LASNEX overestimates the measured profiles by roughly a factor of two over most of the region. The disagreement becomes larger farther away from the slab surface.

Overestimation of the electron density by simulations has been observed in several other experiments involving low-Z CH[5] and high-Z gold disk[12] targets.

For narrower slab widths where we expect large uncertainties, the agreements are actually better. The measured and calculated density profiles agree very well at $x = 0.1$ mm, well within the experimental uncertainty of 0.1 fringe. Near the tip, at $x = 0.05$ mm, where we expect the largest uncertainty due hydrodynamic effects, LASNEX only slightly underestimates the n_e profile.

The disagreement between the simulated and measured n_e profiles may not be entirely due to our inability to accurately model the multi-dimensional hydrodynamic effects. As previously stated, there is some degree of uncertainty in the relative alignment between the laser and the triangular target. This kind of misalignment will change the 2-D modeling geometry used for data analysis in this section. For example, if the center of the laser focus is pointing further away from the tip and the 0.7 mm spot is not tangential to the target tip (see Fig. 2), the actual laser spot at $x = 0.35$ mm will be less than the 0.7-mm slab width used for analysis. This change affects both the amount of laser energy deposited and the 2-D density profile used to get $[n_e]^{cal}$.

In modeling laser-matter interactions, in addition to experimental uncertainties and hydrodynamics, there are many physics mechanisms that can affect the outcome of the simulations. One major uncertainty is the amount of energy deposited by the driving laser due to both inverse bremsstrahlung and resonance absorption.[19] Another study has indicated that the overestimation of the mass-ablation rate can result in a similar density discrepancy.[20] In the near term, we plan to improve both the target geometry and laser uniformity to generate a truly 2-D profile which can be accurately compared to simulations. Given a "calculable" test geometry we can began exploring the validity of various models used in our codes. We are also working on a fully 3-D radiative hydrodynamics code[21] which can properly simulate our geometry.

5. SELENIUM EXPLODING FOIL

To reduce the effect of refraction and to attain high gain in a laser-driven configuration, the exploding-foil technique was designed and employed for achieving the first soft x-ray laser in neon-like selenium.[22,1] Experiments[22,23,12] were performed to test the modeling of the exploding foil and found good agreements between the simulation and n_e profile inferred from Abel inversion of the interferogram. A 0.26-mm probing laser of 20 ns duration was used as the probing source that produced the interferograms.[24] We have repeated the Se exploding foil experiment using the x-ray laser interferometry technique. The shorter wavelength of the yttrium x-ray laser and our optical setup allow us to probe a large area plasma at much higher density and with much better spatial resolution.

In Fig. 7 we show two interferograms showing the plasma evolution in an exploding selenium foil experiment. A 600-ps-long, temporally squared, line focused optical laser incident from the bottom on a 200-nm thick, 1-mm wide (in the z-direction along the x-ray laser probe beam) selenium foil heats and expands the plasma to produce a large hot plasma. The left interferogram is taken near the end of the 600-ps drive pulse (500 ± 100 ps) while the right interferogram was taken at a time (1100 ± 100 ps) long after the end of the driving laser pulse. The fast plasma expansion and subsequent laser burn through is clearly observed.

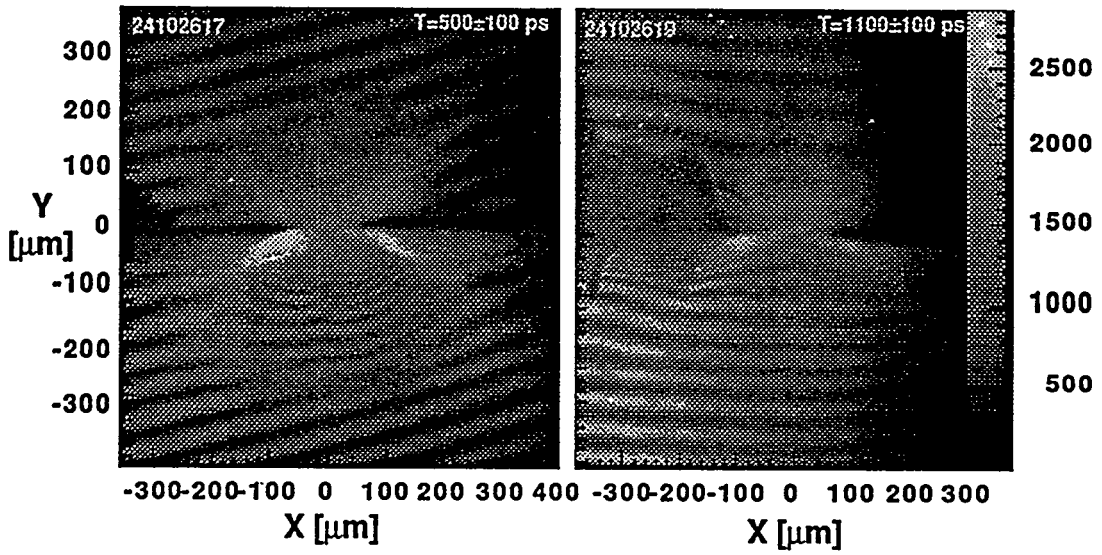

Figure 7 Inteferograms of exploding selenium foil at two different times taken at 15.5 nm. The scale on the right hand side indicates the intensity level of the exposure.

The double-humped structure of the 500 ps interferogram is likely due to the imprinting of non-gaussian spatial distribution of the laser line focus in the *y*-direction. 2-D simulations indicate that we can duplicate the double-humped structure by imposing a 5% intensity depression at the center of the line focus. Such deviation from a perfectly gaussian-shaped spatial distribution is possible since experimentally we achieve the best focus using visual alignment.

Figure 8 is a plot of a snap shot of the 2-D n_e profile at 500 ps into the pulse, at a time within the exposure window for the interferogram shown on the left hand side of Fig. 7. From the 2-D n_e profile we can construct a simulated interferogram, shown in Fig. 9, to compare with the measured interferogram, assuming a plasma length of 1 mm and neglecting the effect of refraction and hydrodynamic expansion along the line focus. We obtained very good agreement between the simulated and measured interferograms.

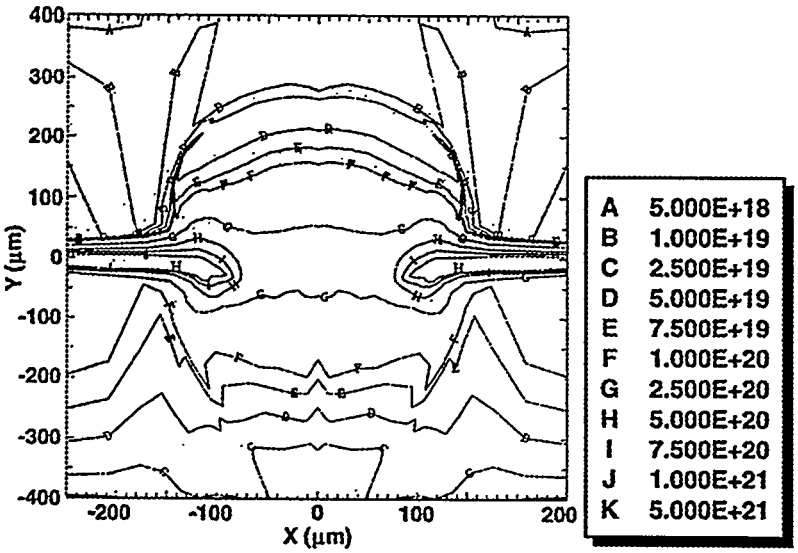

Figure 8. Snap shot of the 2-D electron density profile at 500 ps into the laser pulse.

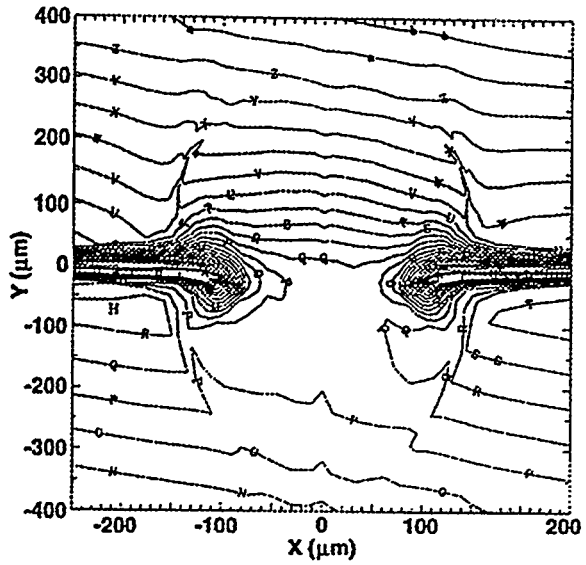

Figure 9. Reconstructed interferogram using the n_e profile shown in Fig. 8, assuming a fixed plasma length of 1 mm and neglecting the effect of refraction and hydrodynamic expansion along the line focus

Taking a cut along the center of the line focus, at $x = 0$, we compare in Fig. 10 the measured n_e profile with profiles obtained from LASNEX simulations at times of 400, 500, and 600 ps into the pulse. The experimental uncertainty is approximately 0.1 fringe, or ~ 1.4 x 10^{19} cm^{-3} (with 1-mm path length). Consider the various assumptions that went into the calculations, on the physics of laser energy deposition via inverse bremsstrahlung and resonance absorptions, on hydrodynamics, and on heat conduction, the agreement is excellent.

6. SUMMARY

The results presented in this paper illustrate the important role soft x-ray laser interferometry can play in diagnosing laser produced plasmas. We have demonstrated that

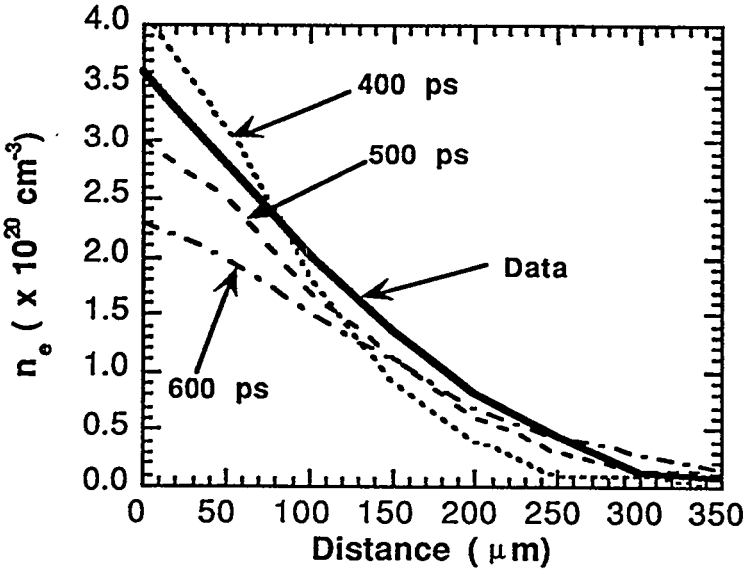

Figure 10. Comparisons between the measured n_e profiles at the center of the line focus ($x = 0$) and profiles obtained from LASNEX simulations at times of 400, 500, and 600 ps into the pulse.

using a soft x-ray laser interferometer we have measured n_e profiles that exceed 10^{21} cm^{-3} for a large plasma that is millimeters in extent. The measured fringe visibility is very good even near the slab surface. Using narrow bandwidth multilayer optics, we observed very little self emission from the plasma.

The triangular target shape allows us to probe a range of plasma path lengths simultaneously. The effect of 2-D hydrodynamic expansion depends on the width of the target. Near the tip of the triangle where the slab is narrow, we expect significant deviation of the measured n_e profiles from nominal 1-D profiles using an infinite slab approximation. We can account for the effect of 2-D expansion by performing 2-D simulations and then averaging the density in the direction transverse to the laser blowoff to arrive at averaged n_e profiles that include the effect of plasma expansion. The calculated n_e profiles gave reasonable agreement with the measured profiles at narrower slab widths, corresponding to positions near the tip of the triangle. For thicker slab widths (400–700 mm), LASNEX overestimates the measurements by a factor of ~2 over most of the plasma. The disagreement is greater as we move further away from the slab surface. The disagreement of the LASNEX calculation with the data suggests further improvements to both the experimental configuration and the method of simulation. We are working on new experiments to remove ambiguities that resulted from complex geometries and experimental configurations. We are also working on expanding the code capabilities and improving physics models used in the codes.

By using a short wavelength x-ray laser as the probe source, we can access a much higher density regime and with better spatial resolution than the previous holographic interferometry experiments performed on selenium exploding foil. We can reconstruct a simulated 2-D interferogram to directly compare with the measured interferogram. Neglecting the effect of plasma expansion along the line focus direction, we can also deduce a spatial n_e profile. We obtained good agreements between the measured and calculated n_e profiles for the selenium exploding foil.

The ultimate motivation of the development of x-ray laser interferometry is to provide a mechanism to probe the deficiencies of our numerical models in areas such as laser deposition by both resonance and inverse bremsstrahlung absorption, flux-limited heat conduction, hydrodynamics, and non-local thermodynamics equilibrium atomic kinetics. The validation and benchmarking of the codes will allow us to gain better understanding of the physics of high-density laser-produced plasmas as we design more and more complex laser experiments such as hohlraum and capsules experiments for ICF applications.

For the next-generation ICF facilities, the experimental emphasis will change from high-rep-rate laser plasma physics research to capsule ignition. The number of experiments will decrease with increasing complexity of the experiments. In order to maximize data return on these complex ICF experiments, each experiment will need to be planned carefully and the need to understand the physics of such ICF capsules and hohlraums will increase. Because of its unique potential, the x-ray laser may be used as a primary diagnostic on many present and future laser plasma experiments.

7. ACKNOWLEDGMENTS

Work performed under the auspices of the U. S. DOE by LLNL under the contract number W-7405-ENG-48 and is partially supported by the Institute Sponsored Research Program.

8. REFERENCES

1. D. Matthews *et al.*, *Phys. Rev. Lett.*, **54**, 110–113 (1985).
2. S. Suckewer *et al.*, *Phys. Rev. Lett.*, **55**, 1753–1756 (1985); S. Suckewer *et al.*, *Phys. Rev. Lett.*, **57**, 1004–1007 (1986).
3. *Proceeding of the Applications of X-ray Lasers Workshop*, R. A. London, D. L. Matthews, and S. Suckewer, ed., Report CONF-9206170, Lawrence Livermore National Laboratory (January 1992).
4. E. Spiller, Soft X-ray Optics (SPIE, Bellingham, WA, 1994).
5. R. Cauble *et al.*, *Phys. Rev. Lett.*, **74**, 3816 (1995).
6. D. Ress *et al.*, *Science*, **265**, 514 (1994).
7. T. W. Barbee Jr. *et al.*, *Appl. Opt.* **32**, 4852-4854 (1993).
8. D. G. Stearns, R. S. Rosen, and S. P. Vernon, *J. Vac. Sci. Technol. A, Vac. Surf. Films* **9**, 2662-2669 (1991).
9. L. B. Da Silva *et al.*, "Electron Density Measurements of High Density Plasmas using Soft X-ray Laser Interferometry," to be published in *Phys. Rev. Lett.* (1995).
10. P. Celliers *et al.*, "Fringe Formation and Coherence of a Soft X-ray Laser Beam Illuminating a Mach-Zehnder Interferometer," submitted to *Opt. Lett.* (May 1995).
11. G. B. Zimmerman and W. L. Kruer, *Com. Plasma Phys. and Cont. Fusion*, **2**, 51 (1975).
12. M. K. Prasad *et al.*, *Phys. Fluids B* **4**, 1569 (1992).
13. D. Ress *et al.*, *Phys. of Fluids B* **2**, 2448 (1990); E. F. Gabl *et al.*, *Phys. Fluids B* **2**, 2437 (1990).
14. A. R. Bell, R. G. Evans, D. J. Nicholas, *Phys. Rev. Lett.* **46**, 243 (1981).
15. J. H. Rogers *et al.*, *Phys. Fluids B* **1**, 741 (1989).
16. W. C. Mead *et al.*, *Phys. Fluids* **26**, 2316 (1983).
17. S. G. Glendinning *et al.*, *Phys. Rev. Lett.* **69**, 1201-1204 (1992).
18. A. S. Wan et al., submitted to *J. Opt. Soc. Am. B*, (March 1995).
19. J. A. Koch *et al.*, submitted to *Phys. Plasmas* (March 1995).
20. R. P. Drake *et al.*, *Phys. Fluids* **31**, 3130 (1988); R. P. Drake, *Phys. Fluids B* **1**, 1082 (1989).
21. D. S. Kershaw, M. K. Prasad, M. J. Shaw, "Three-dimensional Unstructured-mesh Eulerian Hydrodynamics with the Upwind Discontinuous Finite Element Method," to be submitted to *J. Comput. Phys.* (1995).
22. M. Rosen *et al.*, *Phys. Rev. Lett.* **54**, 106–109 (1985).
23. G. Charatis *et al.*, *J. de Physique* **C6**, 89-98 (1986).
24. M. Rosen *et al.*, *Bull. Am. Phys. Soc.*, **27**, 989 (1982); W. B. Fechner et al., *Phys. Fluids* **27**, 1552 (1984).